

# Epitaxial growth of single-domain graphene on hexagonal boron nitride

Wei Yang<sup>1</sup>, Guorui Chen<sup>2</sup>, Zhiwen Shi<sup>1</sup>, Cheng-Cheng Liu<sup>1,3</sup>, Lianchang Zhang<sup>1,4</sup>, Guibai Xie<sup>1</sup>, Meng Cheng<sup>1</sup>, Duoming Wang<sup>1</sup>, Rong Yang<sup>1</sup>, Dongxia Shi<sup>1</sup>, Kenji Watanabe<sup>5</sup>, Takashi Taniguchi<sup>5</sup>, Yugui Yao<sup>3</sup>, Yuanbo Zhang<sup>2</sup> and Guangyu Zhang<sup>1\*</sup>

**Hexagonal boron nitride (h-BN) has recently emerged as an excellent substrate for graphene nanodevices, owing to its atomically flat surface and its potential to engineer graphene's electronic structure<sup>1,2</sup>. Thus far, graphene/h-BN heterostructures have been obtained only through a transfer process<sup>1</sup>, which introduces structural uncertainties due to the random stacking between graphene and h-BN substrate<sup>2,3</sup>. Here we report the epitaxial growth of single-domain graphene on h-BN by a plasma-assisted deposition method. Large-area graphene single crystals were successfully grown for the first time on h-BN with a fixed stacking orientation. A two-dimensional (2D) superlattice of trigonal moiré pattern was observed on graphene by atomic force microscopy. Extra sets of Dirac points are produced as a result of the trigonal superlattice potential and the quantum Hall effect is observed with the 2D-superlattice-related feature developed in the fan diagram of longitudinal and Hall resistance, and the Dirac fermion physics near the original Dirac point is unperturbed. The macroscopic epitaxial graphene is in principle limited only by the size of the h-BN substrate and our synthesis method is potentially applicable on other flat surfaces. Our growth approach could thus open new ways of graphene band engineering through epitaxy on different substrates.**

Among the many graphene synthesis methods, the epitaxial growth approach could help enable large-size and single-domain graphene production in a controlled manner. However, being only one atom thick, graphene is vulnerable to perturbations from its supporting substrate. To access the intrinsic electronic properties of graphene, a substrate that does not disturb its electronic structure is highly desired. This lack of suitable substrate has so far been a major hurdle for the epitaxial growth of graphene. Insulating h-BN has proved to be a superior substrate owing to its atomically flat surface and its lack of charged impurities. Indeed, much improved carrier mobility<sup>1</sup>, fractional quantum Hall effect<sup>4</sup> (QHE) and ballistic transport<sup>5</sup> have been observed in the graphene/h-BN (G/h-BN) heterostructure. So far, most studies<sup>1–5</sup> have dealt with transferred graphene on h-BN substrates, which not only causes the fabrication complexity but also gives rise to structural uncertainties such as lattice orientation, sample uniformity and interface contamination.

Here we present the successful epitaxial growth of single-domain graphene on h-BN. The epitaxial growth is achieved by breaking down the methane molecules with a remote plasma source before the graphene formation on h-BN, thus eliminating the need

for catalysts in contrast to chemical vapour deposition (CVD) growth of graphene<sup>6</sup>. Similar non-CVD approaches for growing 2D materials have been demonstrated for graphene growth on Au (ref. 7) or few-layer h-BN synthesis on graphene/Ru (ref. 8). Our method yields continuous and single-crystalline monolayer graphene (MLG) or bilayer graphene (BLG) films with sizes limited only by the size of the h-BN substrates. As-grown graphene is free from grain boundaries that plagued previous growth attempts<sup>9–11</sup>. Importantly, both MLG and BLG are locked into a fixed orientation with respect to the h-BN substrate, as evidenced by the same uniform trigonal moiré pattern repeated on all of the graphene patches. The moiré pattern, a kind of 2D superlattice, produces extra sets of secondary Dirac points<sup>3</sup> (DPs) that show up unambiguously in our transport measurements. The half-integer QHE in MLG and the 8-fold degeneracy at the zeroth Landau level (LL) in BLG indicate the good quality of both samples, and their undisturbed single-particle band topology near the original DP. It is worth mentioning that LL features of the 2D superlattice were observed with the appearance of new sets of peaks and valleys in the fan diagram of longitudinal and Hall resistance.

To begin with, h-BN crystal flakes with thicknesses from 20 to 120 nm were exfoliated onto a 300-nm-thick SiO<sub>2</sub>/Si substrate by mechanical cleaving<sup>1</sup>. Epitaxial growth of graphene on h-BN was realized at a low temperature  $T \approx 500^\circ\text{C}$  through a remote plasma-enhanced CVD (R-PECVD) process<sup>12</sup> (see Methods). A schematic of the growth process is demonstrated in Fig. 1a, illustrating a typical edge growth of graphene. During growth the feed gas, methane (CH<sub>4</sub>), is dissociated into various reactive radicals, allowing for both nucleation and subsequent growth of graphene at its edges<sup>13,14</sup>; atomic hydrogen, which is also generated in CH<sub>4</sub> plasma, acts as an important etchant for removing amorphous carbon and ensuring  $sp^2$  carbon growth<sup>15</sup>. As-grown graphene was characterized by Raman scattering and the data for MLG and BLG are shown in Fig. 1b. The peak at 1,367 cm<sup>-1</sup> is a characteristic signal of h-BN (ref. 16). The  $sp^2$  graphene nature is evidenced by the G-peak (1,581 cm<sup>-1</sup>) of the spectra<sup>17–19</sup>. Note that the G-peak can split into G<sup>-</sup> (1,564 cm<sup>-1</sup>) and G<sup>+</sup> (1,581 cm<sup>-1</sup>) for hexagonal MLG grains (see Supplementary Fig. S2), revealing zigzag edges of these graphene domains<sup>20,21</sup>. Besides, the 2D peak of MLG is a single Lorentz shape whereas that of BLG is fitted by 4 Lorentz curves (Supplementary Fig. S2), indicating a Bernal stacking for BLG (refs 17–19).

<sup>1</sup>Beijing National Laboratory for Condensed Matter Physics and Institute of Physics, Chinese Academy of Sciences, Beijing 100190, China, <sup>2</sup>State Key Laboratory of Surface Physics and Department of Physics, Fudan University, Shanghai 200433, China, <sup>3</sup>School of Physics, Beijing Institute of Technology, Beijing 100081, China, <sup>4</sup>Department of Physics, Kunming University, Kunming 650214, China, <sup>5</sup>Advanced Materials Laboratory, National Institute for Materials Science, 1-1 Namiki, Tsukuba, 305-0044, Japan. \*e-mail: gygzhang@aphy.iphy.ac.cn

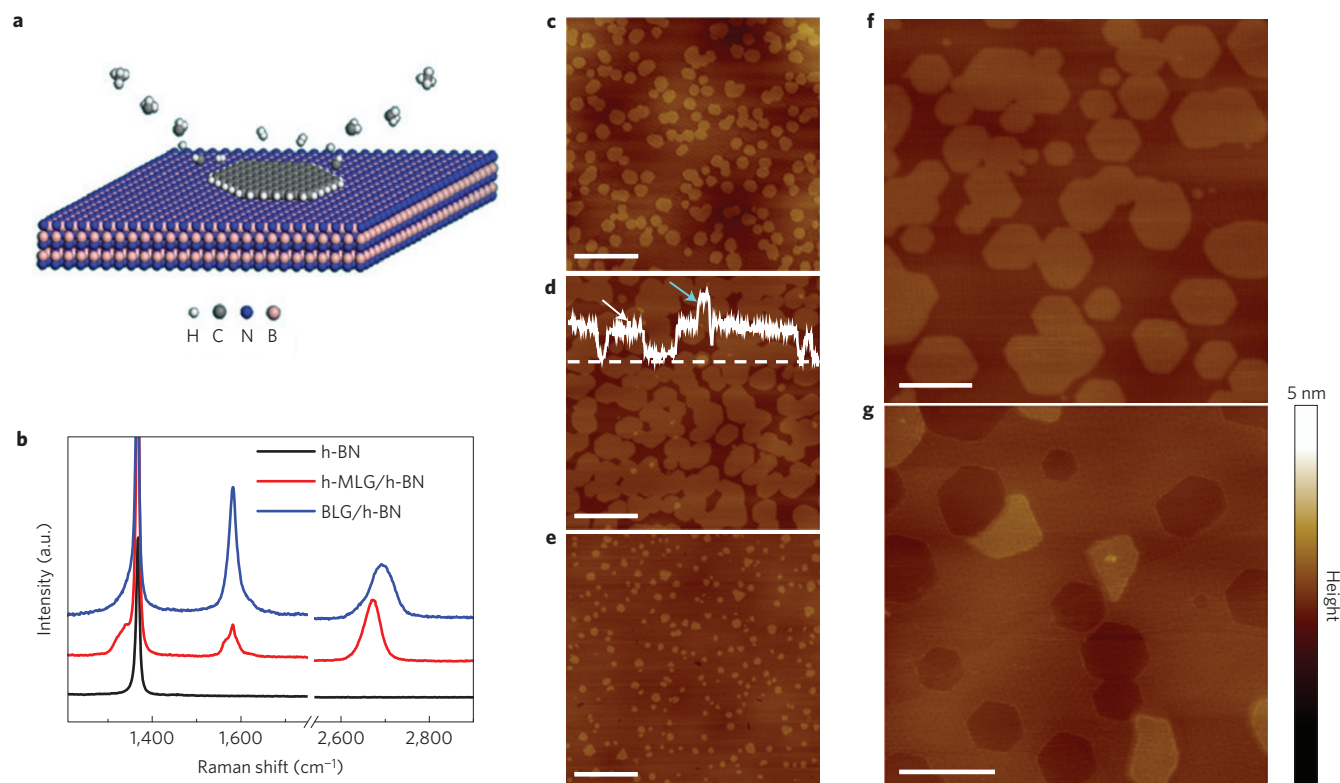


**Figure 1 | Epitaxial graphene growth.** **a**, Schematic illustration of the growth mechanism. **b**, Raman spectra for hexagonal MLG (h-MLG) grains (red), BLG film (blue) and bare h-BN surface (black). **c–e**, AFM images of as-grown graphene on h-BN at different stages including small grains nucleation (**c**), coalescence of grains (**d**), and continuous monolayer graphene with some second-layer nuclei on top. A height profile was extracted along the dashed white line cut in **d**, with white and cyan arrows indicating the first and second layer, respectively. The scale bars in **c–e** are 500 nm. **f, g**, Zoom-in AFM image of as-grown graphene showing aligned hexagonal grains (**f**) or pits after plasma etching (**g**). The scale bars in **f, g** are 200 nm.

For a typical 3-h growth, atomic force microscopy (AFM) imaging (Fig. 1c) revealed small hexagonal grains of graphene uniformly distributed on the h-BN basal plane. These small grains (height  $\sim 0.39$  nm) enlarged and coalesced for longer growth times. Figure 1d shows an AFM image of a sample after 6-h growth, and a height profile is extracted along the white line cut that reveals increased grain size and second-layer (height  $\sim 0.77$  nm) nucleation by white and cyan arrows respectively. Further growth leads to a seamless connection of these grains, forming a continuous and single-crystalline film eventually (Fig. 1e). Note that although there were some additional grains nucleated on top of the bottom layer occasionally, the film was clean, without wrinkles or contamination from the environment.

Importantly, all hexagonal graphene grains have the same orientations (shown in Fig. 1f and Supplementary Fig. S1), indicating that graphene growth on h-BN follows an epitaxy, or more specifically, Van der Waals epitaxy mode<sup>22</sup>. Further evidence for the epitaxial nature of the growth can be seen in Fig. 1g, which was taken after anisotropic etching<sup>15</sup> of a continuous as-grown MLG (see Methods). Hexagonal pits with the same orientations appeared, but no trenches were observed, indicating that the graphene film was free of grain boundaries<sup>15</sup>. As each etched pit originates from a single defect, the low pit density also indicates a low defect density, which we estimated to be  $\sim 10 \mu\text{m}^{-2}$  (see Supplementary Information) in the epitaxial graphene. We also observed continuous graphene growth over a single atomic h-BN step (Supplementary Fig. S3), suggesting that the continuous single-crystalline graphene can be grown on large areas of h-BN surfaces with steps.

As the lattice mismatch between graphene and h-BN is  $\sim 1.8\%$ , we observed moiré patterns of G/h-BN using AFM, which have been

seen previously only by scanning tunnelling microscopy (STM) imaging<sup>2,3</sup>. Figure 2a shows a tapping-mode AFM image of as-grown G/h-BN, revealing a trigonal moiré pattern. To see it clearly, a high-pass-filtered inverse fast Fourier transform of the pattern (for the dashed square in Fig. 2a) was performed. The resulting image (Fig. 2b) yielded a moiré pattern with a periodicity (wavelength,  $\lambda$ ) of  $15 \pm 1$  nm, which is consistent with the modelling result of  $\sim 14$  nm with zero rotation angle<sup>3</sup> (Fig. 2c). Figure 2d–f shows moiré patterns of coalesced hexagonal grains, etched continuous MLG, and continuous BLG, respectively. It is clear that these moiré patterns are well aligned with the zigzag edges of hexagonal MLG grains (Fig. 2d) or etched monolayer pits (Fig. 2e). It was also noted that the universal moiré pattern appears wherever there is graphene, regardless of the number of layers (Fig. 2f and Supplementary Figs S6 and S7). All of these results further confirm the single-crystalline nature of epitaxial graphene on h-BN.

In principle, it is energetically unfavorable to form grain boundaries or line defects during the coalescence of grains with the same lattice orientations. There might be out-of-phase mismatch for the independently nucleated grains during coalescence. However, this out-of-phase mismatch can be possibly relaxed by local lattice distortions or translocations of grains during coalescence by considering the following. Individual grains have relatively large grain sizes, about a few hundred nanometres; and this out-of-phase mismatch is supposed to be very small, less than  $a/2$ , where  $a = 2.46$  Å. Graphene on h-BN has a corrugated superlattice structure. The interaction between graphene and h-BN is weak, causing low friction of graphene on h-BN. Indeed, our STM imaging (Supplementary Fig. S7c–f) on the regions of the coalescence of two graphene grains gives the well-stitched atomic structure, confirming the non-existence of grain boundaries.



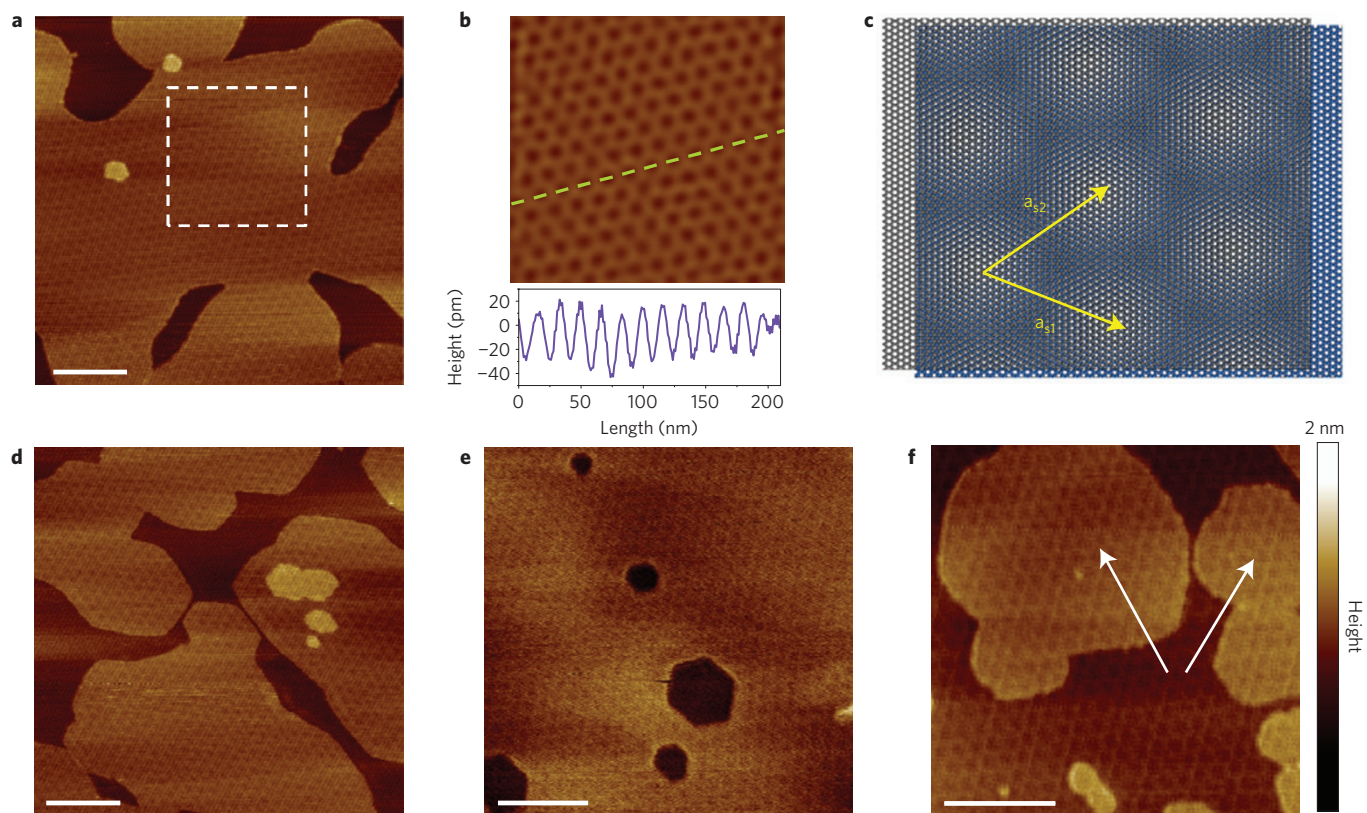


**Figure 2 | Moiré pattern of epitaxial graphene.** **a**, Moiré pattern of a coalesced grain. **b**, High-pass-filtered inverse fast Fourier transform of the pattern in the dashed square in **a**, and the lower part is the height profile along the dashed line. **c**, A schematic illustration of the moiré pattern generated by lattice mismatch with zero rotation angle, the yellow arrows  $a_{s1}$  and  $a_{s2}$  denote the resulting extra lattice (superlattice) structure. **d–f**, Moiré pattern of several grains (**d**), etched MLG (**e**) and BLG (**f**). The white arrows in **f** indicate the third layer. The scale bars in **a, d–f** are 100 nm.

We now turn to the electrical properties of the epitaxial graphene grown on h-BN. Electronic transport measurements were performed on continuous MLG and BLG samples in the Hall bar geometry (see Methods). The resistance of MLG as a function of gate voltage ( $V_g$ ) at different temperatures ( $T$ ) is shown in Fig. 3a, and the mobility extracted from a constant mobility model<sup>4,20</sup> is  $\sim 5,000 \text{ cm}^2 \text{ V}^{-1} \text{ s}^{-1}$  at 1.5 K. For further discussions on the mobility of G/h-BN, see Supplementary Information. Apart from main peak at  $V_g = -33 \text{ V}$  (due to doping from the environment) associated with the DP of pristine graphene, two symmetric satellite peaks appear at both sides of DP. It was noted that the satellite peak in the hole branch is much stronger than that in the electron branch. Such asymmetry can be ascribed to the asymmetry in the on-site energies in the h-BN layer as well as the next-nearest-neighbour interlayer coupling between graphene and h-BN (ref. 3). As  $T$  is lowered, these two extra peaks, as well as the central peak at DP, become more prominent. The insulating behaviour is consistent with that reported on G/h-BN heterostructures obtained by the transfer process<sup>1</sup>. The resistances ( $R$ ) at the DP and satellite peak at the hole branch as a function of  $T$  are plotted in Fig. 3b, and their logarithmic dependence on  $T$  (Fig. 3b) suggests that electron–electron interaction may play a role<sup>23</sup>.

Electronic transport measurements were also performed on continuous BLG samples. The temperature-dependent resistance as a function of  $V_g$  for BLG in Fig. 3c also follows a similar trend as that for MLG. Once again, we observed satellite resistance peaks (Fig. 3c) originating from the moiré pattern, although the magnitude of those in BLG is smaller and becomes barely discernible at  $T > 100 \text{ K}$ .

We attribute the two satellite minimum resistance peaks to the new sets of DPs (ref. 3; superlattice DPs, or SDPs) originating from

the above-mentioned trigonal moiré pattern. To see the connection, we can consider Bragg scattering at the SDP (which corresponds to the  $M^*$  point in the superlattice Brillouin zone<sup>24,25</sup>). As illustrated in Supplementary Fig. S7, the Fermi wavevector  $k_F$  of graphene is given by  $\sqrt{\pi n}$ , where  $n$  is the carrier density; and superlattice period  $\lambda$  gives a superlattice Brillouin zone wavevector at the  $M^*$  point  $G_\alpha = 2\pi/\lambda$ . At the SDP, the Bragg scattering gives  $G_\alpha = 2k_F$ , which leads to  $\lambda = \sqrt{\pi/n}$ , where the carrier density  $n = C_g * \Delta V_g / e$  is approximated by a parallel capacitor model.  $C_g$  is the capacitance, which depends on the thickness of h-BN and  $\text{SiO}_2$ ;  $\Delta V_g$  is the gate voltage difference between the SDP and the DP. Thus, we can roughly estimate  $\Delta V_g = \pi e / (\lambda^2 * C_g)$ . Given that  $\lambda = 13.6 \text{ nm}$  and  $C_g \approx 8 \text{ nF}/\mu\text{m}^2$ , we can get  $\Delta V_g = 34 \text{ V}$ , which matches well with our experimental data. Furthermore, we found that both the amplitude of the satellite peaks and  $\Delta V_g$  are temperature dependent (Fig. 3b and Supplementary Fig. S9). The  $T$ -dependent amplitude variations are most likely due to electron–electron interaction and the interlayer spacing between BN and graphene, which becomes larger when the temperature is increased, leading to a weaker influence of the periodic potential and thus lower satellite resistance peak. The  $T$ -dependent  $\Delta V_g$  shift is most likely due to the decreased capacitance during cooling down (see Supplementary Information for more discussions).

To gain a better understanding of the electrical results, the band structure of the G/h-BN at a zero rotation angle with  $\lambda 13 \text{ nm}$  was calculated using degenerate perturbation theory (for details, see Supplementary Information). The energy dispersion spectrum in superlattice reciprocal space is shown in Fig. 3d, which clearly reveals the presence of extra SDPs beside the original DP. These results agree well with our electronic measurements as well as previous reports<sup>3,24–26</sup>.

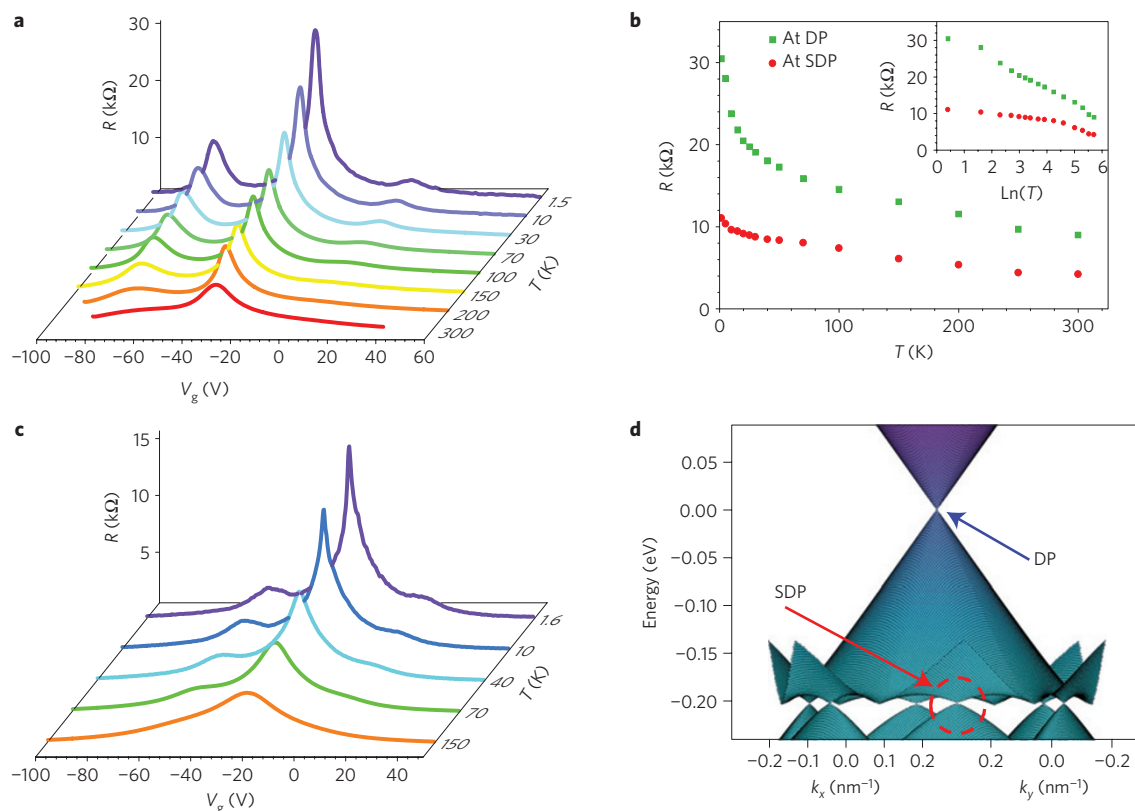


**Figure 3 | Transport measurements and band structure of graphene superlattice.** **a**, Resistance versus applied  $V_g$  at various  $T$  for MLG. **b**, Temperature dependence of the resistance at the DP (green squares) and satellite peaks (or SDP at the hole branch red circles). Inset shows resistance versus natural logarithm of  $T$ . **c**, Resistance versus  $V_g$  at various  $T$  for BLG. **d**, Calculated band structure of graphene epitaxially grown on h-BN with zero rotation angle. The DP and SDP are indicated by blue and red arrows, respectively.

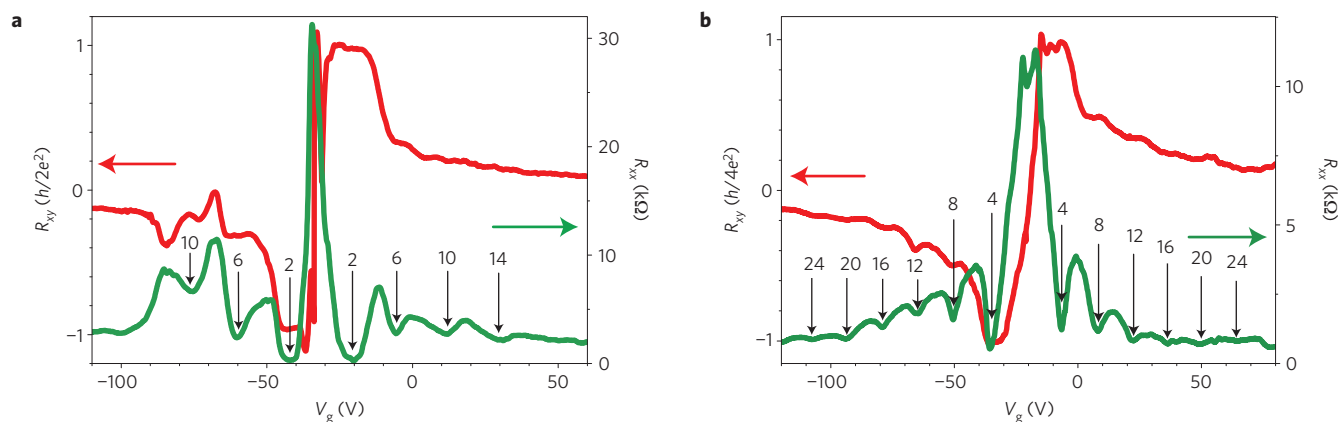


**Figure 4 | QHE of MLG and BLG superlattices.** **a**, Longitudinal ( $R_{xx}$ , green) and Hall resistance ( $R_{xy}$ , red) of MLG versus  $V_g$  at  $T = 1.5$  K,  $B = 9$  T. **b**,  $R_{xx}$  (green) and  $R_{xy}$  (red) of BLG versus  $V_g$  at  $T = 1.6$  K,  $B = 8.8$  T.

We also carried out magnetotransport measurements for the epitaxial G/h-BN heterostructures in the quantum regime at  $T \approx 1.5$  K. The QHE was observed for both MLG and BLG on h-BN, attesting to the good quality of both samples. For MLG, longitudinal resistance ( $R_{xx}$ ) and Hall resistance ( $R_{xy}$ ) as a function of gate voltage taken in a magnetic field of  $B = 9$  T are shown in Fig. 4a.  $R_{xy}$  exhibits well-developed plateaux at filling factors  $\nu = \pm 4(n + 1/2)$  and  $n = 0, 1, \dots$  is the LL index<sup>27–29</sup>, while  $R_{xx}$  vanishes. For BLG,  $R_{xx}$  and  $R_{xy}$  as a function of  $V_g$  at  $B = 8.8$  T are shown in Fig. 4b. The 8-fold degeneracy of the lowest LL in the bilayer is identified by the width of the resistance peak at the DP (ref. 30), which is twice the size of other resistance peaks. It

was found that  $R_{xx}$  at DP begins to split into two as  $B > 6.8$  T (Supplementary Fig. S11c), which suggests emergence of  $n = 0$  LL for BLG.

The  $R_{xx}$  oscillation follows the standard QHE of graphene, and it clearly demonstrates the unaltered Dirac fermion nature of MLG (refs 27,28), even under the heavy influence of the trigonal moiré pattern seen above. However,  $R_{xy}$  behaves abnormally around the SDP in Fig. 4a. There is a sudden drop of  $R_{xy}$  (near to zero) at one side of the SDP and an increase at the other; while  $R_{xx}$  at both sides is a maximum. The change around the SDP is a mimic of that around the DP, which suggests the magnetotransport related to 2D superlattice.

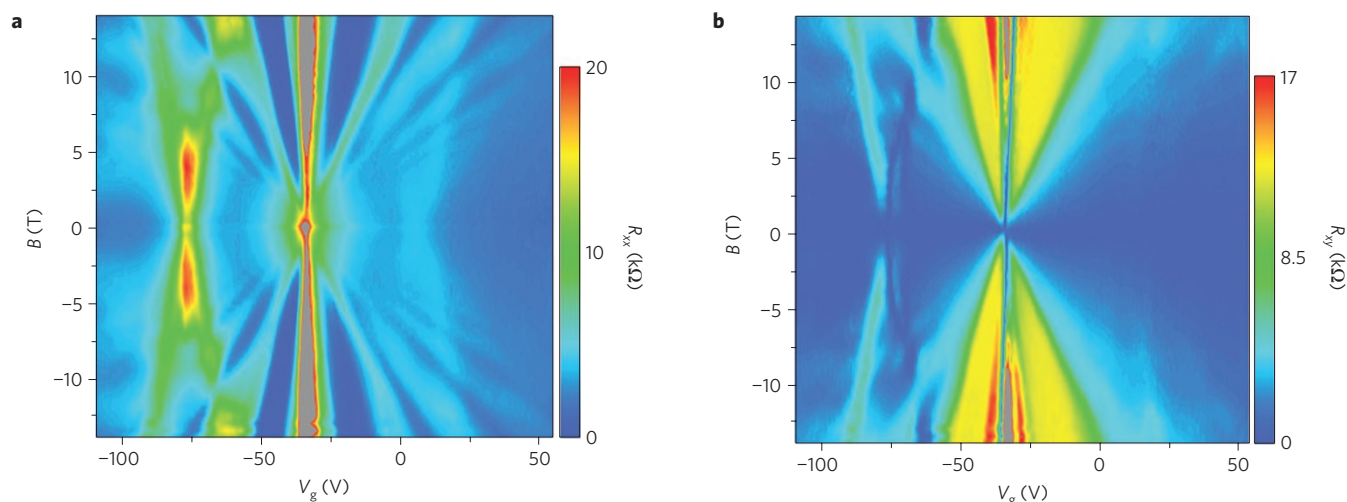


**Figure 5 | QHE fan diagram of MLG superlattice.** **a,b**, Fan diagram of  $R_{xx}$  (**a**) and  $R_{xy}$  (**b**) as a function of  $V_g$  (–110 to 55 V) and magnetic field  $B$  (–14 to 14 T) at  $T = 1.5$  K.

The detailed electronic structure of the DP and the SDP can be seen more clearly in the  $R_{xx}$  and  $R_{xy}$  plotted as a function of both gate voltage and magnetic field. A colour rendering of such a plot is shown in Fig. 5. LLs that are associated with the original DP are clearly observed as peaks fanning out from zero carrier density. The central peak corresponds to the zeroth LL, which is the hallmark of the gapless Dirac spectrum of graphene. Remarkably, similar LLs also developed around the SDP. Close examination of the LL structure at the SDP reveals two important features. First, the central  $n = 0$  LL is absent in the SDP LL sequence. This implies that the energy dispersion at the SDP is gapped. Second, the slope of the  $n = 1R_{xx}$  peak at the SDP coincides with the slope of the  $n = 2R_{xx}$  valley at the original DP (Supplementary Fig. S12). This means a half-filled LL at the SDP has the same number of carriers as that in the half-filled zeroth LL at the DP. The LL degeneracy at the SDP, therefore, equals that at the DP. Both of these features are markedly different from previous theoretical predictions<sup>24,25</sup>, as well as our own tight-binding calculations shown in Fig. 3d, which all point to a gapless dispersion and three times as much LL degeneracy at the SDP compared with that at the DP.  $R_{xx}$  in Fig. 5a also gives a hint of weak localization, as indicated by the resistance peak at  $B = 0$  T. More experiments are underway to address these open questions.

## Methods

**Epitaxial growth of graphene on h-BN.** h-BN flakes were prepared by mechanical exfoliation of BN crystals onto 300-nm  $\text{SiO}_2/\text{Si}$  substrate by Scotch tape. Before growth, the substrate was annealed in hydrogen at 400 °C for 30 min to remove tape residues. Subsequently, the epitaxial growth was carried out by R-PECVD at a substrate temperature of ~500 °C with pure  $\text{CH}_4$  as the carbon source, and the gas pressure and plasma power were 0.2 torr and 100 W, respectively. Usually it takes several growth periods to obtain the desired graphene sample, each period with time about 2 or 3 h. Graphene etching was carried out by R-PECVD at ~350 °C with a flow of  $\text{H}_2$ , plasma power 60 W and time 0.5–1 h. As-grown graphene was characterized by AFM (MultiMode IIIA, Veeco Instruments) using tapping mode at room temperature in ambient atmosphere. STM images were taken in air and at room temperature by a Multi-mode nanoscope SPM system (Veeco). A Pt–Ir alloy tip was used and all atomic resolution images are in constant-height mode. The Raman spectrum was acquired using a micro-Raman microscope (Horiba Jobin Yvon LabRAM HR-800) with an excitation laser wavelength of 532 nm, a power of 1 mW and a beam spot size of ~1  $\mu\text{m}$ .

**Device fabrication and electric measurements for G/h-BN.** As-grown G/h-BN samples were first spin-coated with a polymethylmethacrylate photoresist, followed by electron beam lithography to define the Hall bar structure of graphene, and oxygen plasma etching was used to eliminate the unnecessary parts. A second electron beam lithography process was carried out to define the electrode pattern.

Devices were then fabricated with contact metal (100 nm-Au/2 nm-Ti) deposition through electron beam evaporation and following a standard metal lift-off technique. Before electrical measurements, as-fabricated devices were annealed in a hydrogen atmosphere at 400 °C for an hour to remove resist residues and improve the graphene–electrode contacts. Transport and magnetotransport measurements were carried out in a cryogenic Dewar (Janis and Oxford) using a standard lock-in technique (Stanford).

Received 31 August 2012; accepted 22 May 2013; published online 14 July 2013; corrected online 26 July 2013

## References

- Dean, C. R. *et al.* Boron nitride substrates for high-quality graphene electronics. *Nature Nanotech.* **5**, 722–726 (2010).
- Xue, J. M. *et al.* Scanning tunneling microscopy and spectroscopy of ultra-flat graphene on hexagonal boron nitride. *Nature Mater.* **10**, 282–285 (2011).
- Yankowitz, M. *et al.* Emergence of superlattice Dirac points in graphene on hexagonal boron nitride. *Nature Phys.* **8**, 382–386 (2012).
- Dean, C. R. *et al.* Multicomponent fractional quantum Hall effect in graphene. *Nature Phys.* **7**, 693–696 (2011).
- Mayorov, A. S. *et al.* Micrometer-scale ballistic transport in encapsulated graphene at room temperature. *Nano Lett.* **11**, 2396–2399 (2011).
- Yu, Q. *et al.* Graphene segregated on Ni surfaces and transferred to insulators. *Appl. Phys. Lett.* **93**, 113103 (2008).
- Wofford, J. M. *et al.* Extraordinary epitaxial alignment of graphene islands on Au(111). *New J. Phys.* **14**, 053008 (2012).
- Sutter, P., Lahiri, J., Zahl, P., Wang, B. & Sutter, E. Scalable synthesis of uniform few-layer hexagonal boron nitride dielectric films. *Nano Lett.* **13**, 276–281 (2012).
- Ding, X. L., Ding, G. Q., Xie, X. M., Huang, F. Q. & Jiang, M. H. Direct growth of few layer graphene on hexagonal boron nitride by chemical vapor deposition. *Carbon* **49**, 2522–2525 (2011).
- Son, M., Lim, H., Hong, M. & Choi, H. C. Direct growth of graphene pad on exfoliated hexagonal boron nitride surface. *Nanoscale* **3**, 3089–3093 (2011).
- Tang, S. J. *et al.* Nucleation and growth of single crystal graphene on hexagonal boron nitride. *Carbon* **50**, 329–331 (2012).
- Zhang, L. C. *et al.* Vapour-phase graphene epitaxy at low temperatures. *Nano Res.* **5**, 258–264 (2012).
- Zhang, L. C. *et al.* Catalyst-free growth of nanographene film on various substrates. *Nano Res.* **4**, 315–321 (2011).
- Yang, W. *et al.* Characterization, and properties of nanographene. *Small* **8**, 1429–1435 (2012).
- Yang, R. *et al.* An anisotropic etching effect in the graphene basal plane. *Adv. Mater.* **22**, 4014–4019 (2010).
- Geick, R., Perry, C. H. & Rupprecht, G. Normal modes in hexagonal boron nitride. *Phys. Rev.* **146**, 543–547 (1966).
- Ferrari, A. C. *et al.* Raman spectrum of graphene and graphene layers. *Phys. Rev. Lett.* **97**, 187401 (2006).
- Malard, L. M., Pimenta, M. A., Dresselhaus, G. & Dresselhaus, M. S. Raman spectroscopy in graphene. *Phys. Rep.* **473**, 51–87 (2009).



19. Dresselhaus, M. S., Jorio, A., Hofmann, M., Dresselhaus, G. & Saito, R. Perspectives on carbon nanotubes and graphene Raman spectroscopy. *Nano Lett.* **10**, 751–758 (2010).
20. Shi, Z. W. *et al.* Patterning graphene with zigzag edges by self-aligned anisotropic etching. *Adv. Mater.* **23**, 3061–3065 (2011).
21. Yang, R., Shi, Z. W., Zhang, L. C., Shi, D. X. & Zhang, G. Y. Observation of Raman G-Peak split for graphene nanoribbons with hydrogen-terminated zigzag edges. *Nano Lett.* **11**, 4083–4088 (2011).
22. Koma, A. Van der Waals epitaxy for highly lattice-mismatched systems. *J. Cryst. Growth* **201–202**, 236–241 (1999).
23. Altshuler, B. L., Aronov, A. G. & Lee, P. A. Interaction effects in disordered Fermi systems in two dimensions. *Phys. Rev. Lett.* **44**, 1288–1291 (1980).
24. Park, C.-H., Yang, L., Son, Y.-W., Cohen, M. L. & Louie, S. G. Anisotropic behaviors of massless Dirac fermions in graphene under periodic potential. *Nature Phys.* **4**, 213–217 (2008).
25. Park, C.-H., Yang, L., Son, Y.-W., Cohen, M. L. & Louie, S. G. New generation of massless Dirac fermions in graphene under external periodic potentials. *Phys. Rev. Lett.* **101**, 126804 (2008).
26. Brey, L. & Fertig, H. A. Emerging zero modes for graphene in a periodic potential. *Phys. Rev. Lett.* **103**, 046809 (2009).
27. Novoselov, K. S. *et al.* Two-dimensional gas of massless Dirac fermions in graphene. *Nature* **438**, 197–200 (2005).
28. Zhang, Y. B., Tan, Y. W., Stormer, H. L. & Kim, P. Experimental observation of the quantum Hall effect and Berry's phase in graphene. *Nature* **438**, 201–204 (2005).
29. Gusynin, V. P. & Sharapov, S. G. Unconventional integer quantum hall effect in graphene. *Phys. Rev. Lett.* **95**, 146801 (2005).
30. Novoselov, K. S. *et al.* Unconventional quantum Hall effect and Berry's phase of  $2\pi$  in bilayer graphene. *Nature Phys.* **2**, 177–180 (2006).

### Acknowledgements

The authors would like to thank H. Dai and F. Wang and Y. Yu for helpful discussions. G.Z. acknowledges supports from the 973 Program (2013CB934500 and 2012CB921302), the NSFC (91223204), and the '100 talents project' of CAS. Y.Z. acknowledges supports from the 973 Program (2011CB921802) and NSFC (11034001). Y.Y. acknowledges supports from 973 Program (2011CBA00100) and NSFC (10974231, 11174337 and 11225418).

### Author contributions

G.Z. and Y.Z. designed the research; W.Y. performed the growth, structural characterization, device fabrication and electrical transport measurements; Z.S. helped with QHE measurements; G.C. provided the h-BN substrates and helped with QHE measurements; K.W. and T.T. synthesized h-BN crystals; and C.-C.L. carried out the band structure calculations. W.Y., G.C., Z.S., R.Y., D.S., Y.Y., Y.Z. and G.Z. analysed data; W.Y., G.C., Y.Z. and G.Z. wrote, and all authors commented on, the manuscript.

### Additional information

Supplementary information is available in the [online version of the paper](#). Reprints and permissions information is available online at [www.nature.com/reprints](http://www.nature.com/reprints). Correspondence and requests for materials should be addressed to G.Z.

### Competing financial interests

The authors declare no competing financial interests.

## Epitaxial growth of single-domain graphene on hexagonal boron nitride

Wei Yang, Guorui Chen, Zhiwen Shi, Cheng-Cheng Liu, Lianchang Zhang, Guibai Xie, Meng Cheng, Duoming Wang, Rong Yang, Dongxia Shi, Kenji Watanabe, Takashi Taniguchi, Yugui Yao, Yuanbo Zhang and Guangyu Zhang

*Nature Materials* <http://dx.doi.org/10.1038/nmat3695> (2013); published online 14 July 2013; corrected online 26 July 2013.

In the version of this Letter originally published online, the year of the received date should have read '2012'. In Fig. 5, the numbers 10, 20, 8.5 and 17 on the colour scale bars should not have been followed by 'k'. These errors have been corrected in all versions of the Letter.